Bubble Nucleation and Growth in Nanochannels

Bo Bao, Seyed Hadi Zandavi, Huawei Li, Junjie Zhong, Arnav Jatukaran, Farshid Mostowfi, David Sinton

UNIVERSITY OF TORONTO LIBRARIES

Journal Name

ARTICLE

Bubble Nucleation and Growth in Nanochannels

Bo Bao[a,†], Seyed Hadi Zandavi[a,†], Huawei Li[a], Junjie Zhong[a], Arnav Jatukaran[a], Farshid Mostowfi[b], David Sinton[a,*]

We apply micro- and nanofluidics to study fundamental phase change behaviour at nanoscales, as relevant to shale gas/oil production. We investigate hydrocarbon phase transition in sub-100 nm channels under conditions that mimic pressure drawdown process. Measured cavitation pressures are compared with those predicted from the nucleation theory. We find that cavitation pressure in the nanochannels corresponds closer to the spinodal limit than that predicted from classical nucleation theory. This deviation indicates that hydrocarbons remain in the liquid phase in nano-sized pores under pressures much lower than the saturation pressure. Depending on the initial nucleation location – along the channel or at the end – two types of bubble growth dynamics were observed. Bubble growth was measured experimentally at different nucleation conditions, and results agree with a fluid dynamics model including evaporation rate, instantaneous bulk liquid velocity, and bubble pressure. Collectively these results demonstrate, characterize, and quantify isothermal bubble nucleation and growth of a pure substance in nanochannels.

Introduction

Global energy has been reshaped by the rapid emergence of hydrocarbon production from nanoporous shale and tight oil reservoirs[1,2]. The pores in shale and tight oil formations are mostly nano-sized (few to tens of nanometers, e.g. the dominant pore size in the Bakken shale[3], and the Pierre shale[4] range from 60-110 nm and 40-90 nm, respectively), necessitating fundamental understanding of fluid phase and transport properties of nanoconfined reservoir fluids, particularly as pressurization and depressurization alter the phase state[5–7]. The fundamental physics governing phase change at the nanoscale remains poorly understood, and the available classical theories and simulation techniques have proven inadequate[5].

Liquids at temperatures above (or pressures below) the saturation become metastable and susceptible to transform to a stable vapor phase via vapor bubble nucleation (cavitation or boiling)[8]. A review of experimental approaches for measuring the limit of metastability of liquids in the bulk/macro systems can be found elsewhere[9,10]. The classical nucleation theory is typically used to study the fundamental physics of bubble nucleation in a pure liquid. Significant discrepancies between experimental results and classical homogeneous nucleation theory have been reported [11,12]. These discrepancies are usually attributed to the differences in surface tension[13,14] or the existence of different types of heterogeneity in the system such as surface roughness and channel corrugations [11,14,15], heterogeneity in wetting[11,12,16], external perturbations [11], and/or the presence of bubbles or particles[11].

The rupture of the metastable liquid phase occurs by the nucleation of a nano-sized bubble. Therefore, investigation of the stability of the liquid at nanoscale is crucial. Many investigations of liquid-vapor phase change in nanoscale were carried out by measurement of adsorption[17,18], by interferometry[19] or through surface force apparatus[20]. Recent advances in micro- and nanofluidics techniques allow direct investigation of fluid flow and phase transition in deterministic structures at this scale [21,22]. Microfluidics has been applied to a variety of phase measurements including Dew point,[23] gas-oil-ratio [24] and more recently the whole Pressure-Temperature phase diagram was mapped on a single chip [25], although these studies focused on equilibrium measurements at microscales. Ando et al.[26] reported homogeneous bubble nucleation achieved by a laser-induced shock on a free surface in micro-fluidic channels. Nagashima et al.[27] detected a single bubble nucleation in a single nanopore with the radius of 43.5 nm by extreme pulsed superheating. Vincent et al.[28] observed the bubble nucleation and growth during the drying process of water in the ink-bottle nanostructure and found that the liquid phase pressure at cavitation was less negative than that expected from the nucleation theory. Witharana et al.[29] found that larger micrometer-sized cavities nucleate vapor at a lower superheated temperature than smaller nanometer-sized cavities. Duan et al.[30] reported evaporation-induced cavitation of water in 20-120 nm deep nanochannels. Collectively these relatively recent results indicate a rich and complex physics, deviating significantly from bulk behavior.

[a.] Department of Mechanical and Industrial Engineering, University of Toronto, M5S3G8 Canada.

[b.] Schlumberger-Doll Research, Cambridge, Massachusetts, 02139 USA.

* sinton@mie.utoronto.ca

† Bo Bao and Seyed Hadi Zandavi contributed equally to this work.

In this paper, we apply micro- and nanofluidics to study the liquid-to-vapor phase transition of propane in sub 100-nm confinement. The chip allows direct visualization of bubble nucleation and growth. The measured nucleation temperatures and pressures are compared with nucleation theory. We also investigate the growth rate of vapor bubble column after nucleation. Two

growth mechanisms are distinguished, with results compared to a fluid dynamics model for evaporation rate, liquid velocity, and bubble pressure.
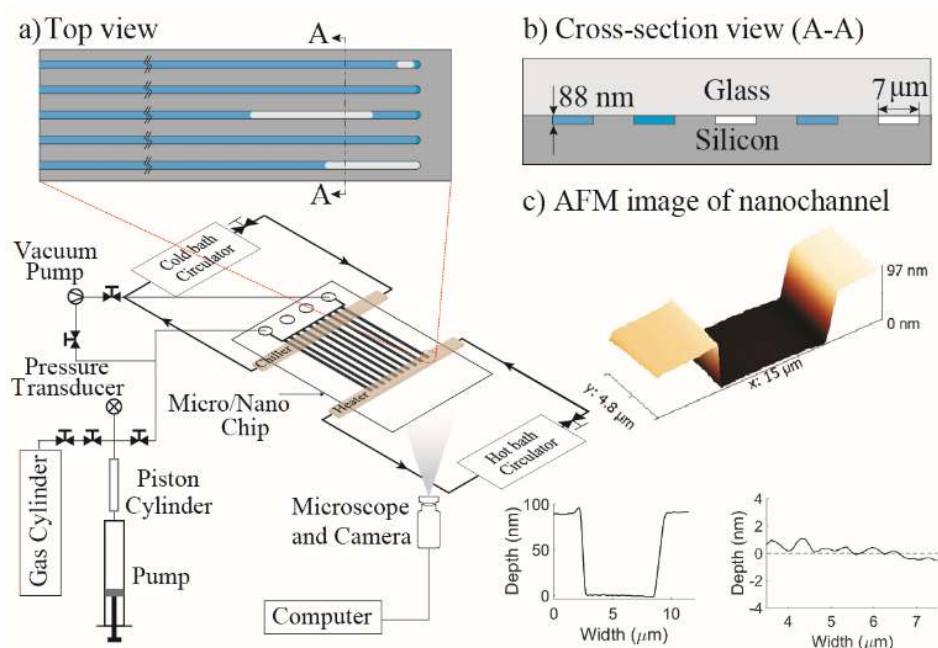

Fig. 1 a) Schematic of the experimental setup including micro/nanofluidic chip and top view of the chip; b) Schematic of cross-section view of 88-nm deep nanochannels; c) Typical AFM profile of a nanochannel. Each channel has a width of 7 μm and depth of 88 ± 3 nm. The top image is a topological scan of one channel. The left image shows the depth profile of a single channel and the right image is the relative roughness of the channel.

Method

A schematic of the experiment is shown in Fig. 1. The test region consists of 10 identical dead-ended nanochannels of 88-nm depth (7 μm × 35 mm). The nanochannels are fabricated by deep-reactive-ionic-etching on a silicon wafer and anodic bonding with glass. The nanochannels were characterized using atomic force microscopy (AFM) prior to glass bonding. The channel depth was ~ 88 ± 3 nm with little surface roughness, ~ 1 nm, along the channel length. AFM results are included in Fig. 1, and full chip fabrication and characterization details are provided in Electronic Supplementary Information, Sections S2 and S3.

The assembled nanofluidic chip is mounted on a customized manifold enabling appropriate sealing for high pressures. The chip and manifold are connected to a sample source cylinder (research grade propane, Praxair 99.99%), pump (TELEDYNE ISCO MODEL 260D), and piston cylinder (HIP 70C3-10-P) via tubing and valves. During this process, the temperature and pressure are well maintained and monitored. To ensure nucleation occurs within the bulk liquid phase instead of the liquid-vapor interface [16,] we directly control the local temperature difference on the chip with a heater and chiller clamped on top of the chip. The dead-end portion of the nanochannel (~5 mm) is maintained uniformly at a higher temperature (T_{high}), while the entrance portion (near the inlet port) is kept uniformly at a lower temperature (T_{low}). The field of view (~ 1

mm) falls into the T_{high} region (~ 5 mm). The heater and chiller are copper-made blocks with water / silicone oil circulated from a temperature-controlled bath. Both the heater and the chiller were in close contact with the silicon side of the chip to minimize contact thermal resistance. The temperature in the heater region (dead-end region) was controlled by circulating hot water/silicone in the copper block heater, which covered the last 5 mm length of the nanochannels (the total length of the chiller was 10 mm). The maximum gradient in the heater region was 0.1 K over the 1 mm field of view, therefore, the bubble nucleation and growth was assumed to be isothermal in the field of view (see Supplementary Information for the details of temperature measurement). Pressure is provided and controlled (± 0.5% accuracy) by the pump and monitored by a pressure transducer (PX409-3.5KGUSBH) near the chip. An isolation piston cylinder is used between the pump and chip to avoid contamination of the sample.

The tubing, pump, piston chambers and valves are cleaned thoroughly and connected to the micro / nanofludic chip. The entire system is vacuumed for 15 minutes. Research-grade propane is filled into the nanochannels. Isothermal cavitation tests are performed systematically, with T_{high} and T_{low} kept constant and pressure initially set far above the saturation pressure at T_{high}. We waited 1 hour to reach steady-state thermal conditions. Pressure is then decreased in steps. We waited for 15 minutes at each pressure step to observe bubble nucleation. Cycles are repeated until bubble nucleation

occurs. Bubble nucleation and growth are visualized in bright-field mode using an inverted microscope (LEICA DMI 6000B) mounted with a 10× objective lens. The vapor and liquid phases were clearly distinguished by light intensity: the vapor phase appeared bright while the liquid phase appeared darker. The details of experimental procedure and temperature measurements are shown in Supplementary Information (Sections S4 and S5).

Results and discussions

Bubble Nucleation

In total, cavitation experiments at eight different temperatures between T_l = 342.4 K and 375.9 K are performed. The measured value of the cavitation pressures $\Delta P_{cav} = P_{sat}(T_l) - P_l$ and the corresponding superheat $\Delta T_{sup} = T_l - T_{sat}(P_l)$ are provided in Supplementary Information, Section S5. The superheating and cavitation measurements along with the saturation curve are shown in the phase diagram of propane in Fig. 2. The dependence of the cavitation pressure on liquid phase temperature has been obtained. The maximum value of the superheat measured in the experiments is ΔT_{sup} = 31.6 K at P_l = 1.30 MPa. Similarly, the maximum value of cavitation pressure in the experiments is ΔP_{cav} = 1.26 MPa at T_l = 342.4 K. The values of ΔT_{sup} and ΔP_{cav} decrease as the experimental condition moves toward the critical point of propane. Each measurement point in Fig. 2 is a result of the average of at least three independent, repeated cavitation-experiments in two separate micro/nanofluidic chips.

The cavitation process initiates by an explosive growth of seeding bubbles in liquids [11]. The necessary conditions for thermodynamic equilibrium lead to an expression for the critical radius, R_c. When the radius of a nuclei bubble is bigger than R_c, it can grow unlimitedly[31]. For a nanochannel, a necessary, but not sufficient, condition for bubble nucleation is $2R_c < Min(h,w)$, where h and w are the channel depth and width [32]. For propane in a nanochannel with a depth of h = 88 nm, the minimum superheating (cavitation) required can be calculated from the Kelvin equation, which can be expressed as [33]:

$$R_c = \frac{2\,\gamma(T_l)}{P_{sat}(T_l)\exp\left[\frac{1}{\rho_l k_B T}(P_l - P_{sat}(T_l))\right] - P_l}, \qquad (1)$$

where γ is the liquid-vapor surface tension; k_B and ρ_l are the Boltzmann constant and the density of the liquid at the saturation condition, respectively. Here, the minimum superheating required calculated from eqn (1), with $R_c = h/2$, is plotted in Fig. 2. As shown, the Kelvin saturation line corresponds closely to the bulk propane saturation line – indicating that the minimum superheating condition in the 88-nm channel is not significantly influenced by the channel dimensions.

The kinetic limit of the metastable liquid phase or the onset of homogeneous nucleation can be obtained from the classical nucleation theory [11]. The liquid phase cannot remain in a metastable state for an arbitrarily long period of time and the nucleation theory predicts the time, t_N, for which a liquid can be held at pressures below (or temperatures above) the saturation, before the first bubble nucleation would be expected from the motion of the molecules in the bulk liquid phase. Here, a simple form of nucleation theory is used to obtain the nucleation pressure, P_N^L, [33]

$$P_N^L = \eta P_{sat}(T_l) - \left[\frac{16\pi\gamma^3}{3k_B T_l \ln(ZV_l t_N)}\right]^{\frac{1}{2}}, \qquad (2)$$

where V_l is the volume under observation, t_N the nucleation time and η is simply

$$\eta = \exp\left[\frac{1}{\rho_l k_B T_l}(P_l - P_{sat}(T_l))\right].$$

In eqn (2), Z is the rate constant and estimated to be 25×10^{30} (cm³ s)$^{-1}$ [33]. As can be seen in Fig. 2, the nucleation theory over predicts the cavitation pressures, given a waiting time of t_N = 900 s and an observation volume of 88 nm × 7 µm × 1 mm.
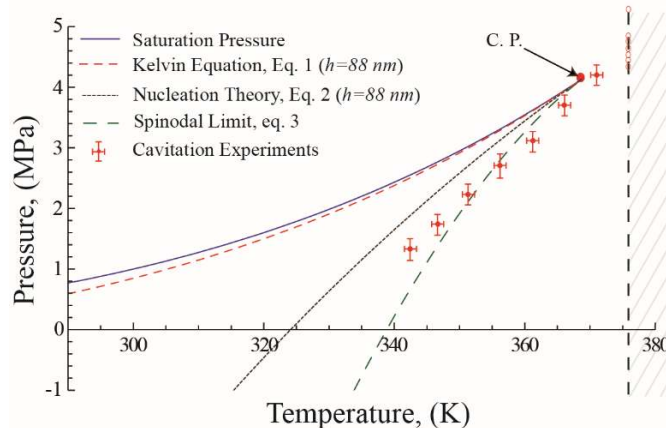

Fig. 2 Measurements of bubble nucleation in 88-nm deep nanochannels. Plotted for comparison are the saturation vapor pressure, capillary pressure calculated from the Kelvin Equation, eqn (1), the prediction from the classical nucleation theory, eqn (2) for t_N= 900 s, and the spinodal limit from eqn (3).

In general, for a liquid that completely wets a solid substrate such as propane (contact angle ~ 0), nucleation is expected to occur slightly below the homogeneous nucleation theory prediction (less superheat)[34,35]. Previous experimental results for bulk propane showed that the maximum measured nucleation temperature at atmospheric pressure was 326.1 K while the homogeneous nucleation theory predicts a boiling temperature of 328.5 K[35]. The early onset of nucleation usually found at larger scales is generally attributed to surface roughness and wetting characteristics. However, our results demonstrate a delayed bubble nucleation in nanochannels that is shifted beyond the classical homogeneous nucleation prediction. The maximum deviation is ~ 4 K and this deviation decreases as the experimental conditions approach the critical point. This deviation is not the result of wetting characteristics since propane fully wets the silicon-glass surfaces.[36] The deviation is also not attributed to nanochannel roughness since the AFM image shows a relatively low roughness of ~ 1 nm (See section S3 of Supplementary Information for details on the nanochannel roughness). The deviation here is attributed to nanoconfinement.

The theoretical extreme limit of the metastable liquid is the spinodal limit (liquid spinodal); the point at which the slope of the P-V phase diagram at a constant temperature, $(dP/dV)_T$, changes from negative to positive.[11] The line joining the minima is called the liquid spinodal line and it ends at the critical point.[11] The regions between the classically-predicted liquid spinodal lines and the saturated lines are of particular interest because, only the metastable phase should be present in this region. Beyond this limit the liquid phase becomes unstable. In this work the Furth formula for the spinodal limit is used: [37]

$$P_{sp}(T_l) = P_{sat}(T_l) - 1.32\,\gamma^{\frac{3}{2}}(3k_B T)^{\frac{1}{2}}. \qquad (3)$$

This equation has been shown to work well in the region of positive pressures and in the region close to the critical point[38]. The green, dashed line in Fig. 2 shows the spinodal limit of liquid propane calculated from eqn (3). As shown in Fig. 2, three of seven nucleation measurements lay between the prediction from the classical nucleation theory and the spinodal limit, while four of them exceed the spinodal limit.

Although the shift in critical point is not the main focus of this work, we continued the isothermal nucleation experiment by increasing the temperature beyond the critical point with the similar step size in temperature. The difference of the reflective light intensity between vapor and liquid decreased as the measurements moved towards the critical point (quantified in Supplementary Information, Section S6). At 375.9 ± 1 K no liquid to vapor phase transition was observed (vertical, dashed line in Fig. 2). The last detected nucleation point (T_I = 371.0 ± 1 K) is only ~ 1.3 ± 1 K higher than the critical point (369.7 K). Thus while the nucleation experiments here demonstrate significant shift from classical nucleation theory, no significant critical point shift was detected.

Bubble Growth

Following nucleation of a vapor bubble, a vapor column grows in the nanochannels. A high-speed camera (PCO 1200S) connected to the inverted optical microscope (LEICA DMI 6000B) with a sampling speed of 50 frames per second is used to observe the bubble growth process in the test region of the nanochannels. In all the cavitation tests, we observed two types of bubble column growth mechanisms according to the location of bubble nucleation: Type A where the bubble nucleates at channel-end, and Type B where the bubble nucleates along the channel. Figs. 3a and 3b show image sequences of Type A and B growth at a particular nucleation condition, respectively. (The Supplementary video shows examples of Type A and Type B growth.)

The bubble column length and liquid-vapor interface positions are extracted from image sequences using an image processing algorithm. As shown in Fig. 3c, Type A growth experiences two regimes, namely "transient start-up" and "steady linear growth". In the case shown in Fig. 3c, the transient start-up regime takes about 200 ms. In this figure, l_B is defined as vapor bubble column length. The velocity of liquid-vapor interface (vapor bubble column growth rate) is initially high (~ 4.6 μm/ms), and becomes slower afterward. The transient start-up regime smoothly transitions into the steady linear growth regime, where the bubble column grows at a lower and constant velocity of ~ 0.32 μm/ms.
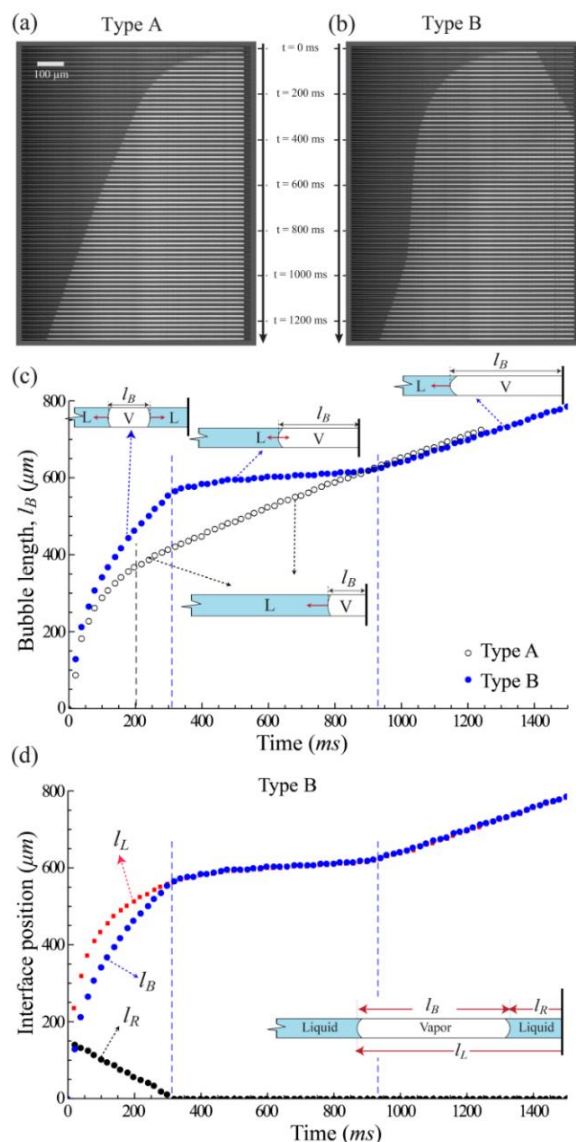

Fig. 3 Mechanisms of bubble column growth at Tl = 346.3 K and Pl = 1.60 MPa: a) Image sequence of Type A growth where vapor bubble nucleates at channel-end; b) Image sequence of Type B where vapor bubble nucleates along the channel; c) Bubble length l_B versus time of Type A and B growth; d) Positions of left and right liquid-vapor interfaces, l_L and l_R, of Type B growth.

In contrast, the Type B growth curve presents three different regimes, namely "transient start-up", "transitional" and "steady linear growth" regimes, as shown in Fig. 3c. In the Type B growth, Fig. 3b, both the right and left interface movement contribute to the vapor bubble column growth. Therefore, both left and right interface positions are tracked, as shown in Fig. 3d. In this figure, l_L and l_R are defined as the distance between the channel-end and the left and right liquid-vapor interfaces, respectively. The vapor bubble length is simply $l_B = l_L - l_R$ (Fig. 3d).

In the transient start-up regime, while the right liquid-vapor interface moves at a constant velocity, the left liquid-vapor interface moves non-linearly, similar to Type A in the transient start-up regime. When the right liquid-vapor interface hits the channel-end (l_R = 0), there is a significant slowing in the bubble growth – an effective pause prior to subsequent steady linear growth (Fig. 3d). We term this ~ 0.62 s period the transitional regime, which is unique to Type B growth. It is seen that l_B could grow slightly, or remain

unchanged, or even shrink in this regime depending on the experimental conditions (examples of both Type A and B growth at other nucleation conditions are presented in Supplementary Information, section S8). Previous experimental studies [39, 40] have also reported a variety of dynamics in the growth and collapse of bubbles in microtubes and microchannels. In those experiments, vapour bubbles appear rapidly in the system as a result of short heat pulses. The exact mechanisms governing the bubble shrinking dynamics observed in the transitional regime of Type B growth here, however, remain an open question. Finally, in the steady linear growth regime, the bubble column grows at a constant velocity (0.32 µm/ms), which is equal to the velocity of the steady linear growth regime in Type A growth.

Surprisingly, for each of the nucleation conditions, the bubble growth curves converge eventually in steady linear growth regime regardless of type or initial nucleation location, Fig. 3c. That is, while Type A and B growth show distinct dynamics in earlier times, the ultimate interface position and rate of advance are the same for both cases once in steady linear growth regime. As shown in Fig. 3c, the liquid-vapor interface for the two growth types reach the same position (620 ± 10 µm) after 870 ms from the time of nucleation (See Supplementary Information for other experimental conditions).

Fig. 4a shows Type A growth of the vapor bubble column at different nucleation conditions. In order to show the data clearly, only one channel is selected as representative at each temperature. As shown, the growth of Type A in the nanochannels depends on both temperature and pressure in the liquid phase. A fluid dynamics model is developed to determine the evaporation rate dN_v/dt, liquid velocity $u_{liq}(t)$, and bubble pressure during bubble growth $P_v(t)$. The bulk liquid flow in the nanochannel is approximated as one-dimensional flow. A schematic diagram of a simple one-dimensional model of the system is shown in the inset of Fig. 4b. Following the detailed description outlined in the Supplementary Information (Section S7), the governing equation of the liquid motion in the nanochannel is: [39]

$$D_l \rho_l \frac{du_{liq}(t)}{dt} + f u_{liq}(t) = P_v(t) - P_{res}; \quad (4)$$

where D_l is the distance from the liquid-vapor interface to the reservoir, f is the flow friction, and P_{res} is the reservoir pressure. The governing equationn of the vapor bubble is:

$$\frac{dl_B(t)}{dt} = \frac{RT}{AP_v(t)}\frac{dN_v(t)}{dt} - \frac{l_B}{P_v(t)}\frac{dP_v(t)}{dt} \quad (5)$$

where where N_v is the moles of vapour and A is the cross sectional area of the nanochannel.
The continuity equation at the liquid vapor interface is:

$$\frac{dl_B(t)}{dt} = u_{liq}(t) + \frac{M}{A\rho_l}\frac{dN_v(t)}{dt}, \quad (6)$$

where M is the propane molar mass.

The differential equations (4) to (6) form a coupled system with three unknowns; $u_{liq}(t)$; $N_v(t)$; and $P_v(t)$. Solving the equations requires a boundary condition and assumptions on $u_{liq}(t)$, $N_v(t)$, or $P_v(t)$ (see the Supplementary Information, Section S8).

The inset in Fig. 4a shows that the evaporation rate, dN_v/dt, calculated from the model. As shown, the evaporation rate decreases from 2.02 x 10^{-13} to 0.99 x 10^{-13} mol/s as the temperature increases (superheat decreases). Having the evaporation rate, it is found that on average ~87% of the liquid-vapor interface movement, $dl_B(t)/dt$, results from the liquid flow, $u_{liq}(t)$, and the remaining is due to evaporation, dN_v/dt. The ratios at different nucleation conditions are: 90% (342.4 K), 88% (346.3 K), 88% (351.3 K), 86% (356.2 K) and 84% (361.2 K).
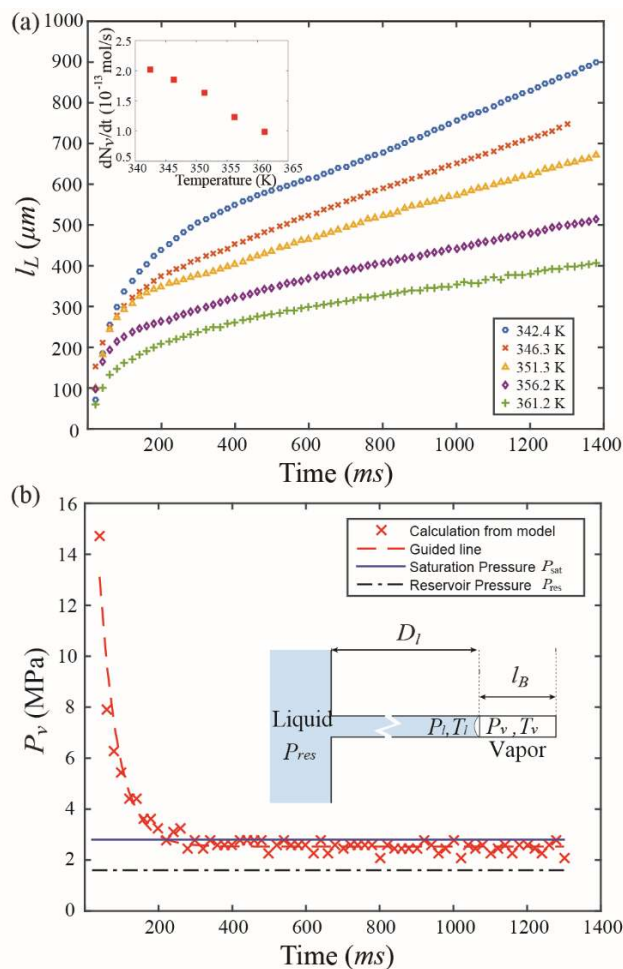

Fig. 4 a) Bubble length, lB(t), of Type A at different nucleation conditions; inset shows the calculated evaporation rate dNv/dt in steady linear growth regime; b) The calculated pressure in the vapor phase P_v versus time in the bubble nucleation test at T_l = 346.3 K.

Fig. 4b shows the predicted vapor pressure in the bubble as a function of time for the Type A nucleation in Fig. 3. The bubble pressure is predicted to be as high as 14.7 MPa initially (indicating that bubble expansion is governed by the balance of pressure force and surrounding fluid inertia[41]) and dropping sharply approaching a plateau level of 2.52 MPa in the steady linear growth regime. The transient regime of P_v agrees with the general trend observed previously for growth and collapse of a vapor bubble column with transient heating in a microtube [22]. (See Supplementary Information for P_v at other nucleation conditions)

The calculated P_v in the steady linear growth regime is found to be ~14 % on average lower than P_{sat} at different nucleation conditions: 14% (342.4 K), 10% (346.3 K), 13% (351.3 K), 17% (356.2 K), and 14% (361.2 K). The somewhat lower prediction of pressure (P_v) is an indication of higher viscous friction in the nanochannels as compared to the theoretical value. Previous studies have also shown that the predicted values of the velocity from one-dimensional theoretical models are higher than the actual measured values in nano-confinement[42,43]. In general, this phenomenon has been attributed to surface roughness, the presence of bubbles, and/or the formation of highly viscous layers near the interface[42,44,45,46]. The maximum deviation (17%) observed here is relatively small as compared to reported values for water, ethanol, and isopropanol in nanochannels[43,47].

Conclusions

In this paper, we apply micro- and nanofluidics to study the fundamentals of liquid-to-vapor phase transition of a nanoconfined hydrocarbon. Propane phase transition in 88-nm channels was investigated with conditions mimicking the isothermal pressure drawdown process in shale gas/oil production. In contrast to the bulk phase, it is found that the cavitation pressure in the nanochannels corresponds closer to the spinodal limit than that predicted by classical nucleation theory. The implication is a significantly greater delay in gas production from nanoconfined liquids as compared to existing theory.

For the growth of the vapor column following nucleation, two different growth mechanisms are distinguished depending on the location of the bubble nucleation. Finally, a fluid dynamics model is developed to determine the evaporation rate, liquid velocity, and bubble pressure during bubble growth. Collectively these results demonstrate, characterize, and quantify isothermal bubble nucleation and growth of a pure substance in nanochannels which will be beneficial in understanding many natural processes and optimizing related applications.

Acknowledgement

References

1   D. Malakoff, *Science (80-.).*, 2014, **344**, 1464–1467.
2   T. W. Patzek, F. Male and M. Marder, *Proc. Natl. Acad. Sci. U. S. A.*, 2013, **110**, 19731–19736.
3   S. Zargari, K. L. Canter and M. Prasad, *Fuel*, 2015, **153**, 110–117.
4   U. Kuila and M. Prasad, *Geophys. Prospect.*, 2013, **61**, 341–362.
5   L. Cueto-Felgueroso and R. Juanes, *Proc. Natl. Acad. Sci.*, 2013, **110**, 19660–19661.
6   P. J. M. Monteiro, C. H. Rycroft and G. I. Barenblatt, *Proc. Natl. Acad. Sci.*, 2012, **109**, 20309–20313.
7   B. Bai, M. Elgmati, H. Zhang and M. Wei, *Fuel*, 2013, **105**.
8   T. D. Wheeler and A. D. Stroock, *Nature*, 2008, **455**, 208–212.
9   F. Caupin and E. Herbert, *Comptes Rendus Phys.*, 2006, **7**, 1000–1017.
10   C. T. Avedisian, *J. Phys. Chem. Ref. Data*, 1985, **14**, 695–729.
11   C. E. Brennen, *Cavitation and bubble dynamics*, Oxford University Press, Oxford, 1995.
12   I. T. Chen, D. A. Sessoms, Z. M. Sherman, E. Choi, O. Vincent and A. D. Stroock, *J Phys Chem B*, 2016, **120**, 5209–5222.
13   N. Bruot and F. Caupin, *Phys. Rev. Lett.*, 2016, **116**, 1–5.
14   M. E. M. Azouzi, C. Ramboz, J.-F. Lenain and F. Caupin, *Nat. Phys.*, 2013, **9**, 38–41.
15   T. Hoffman, D. Wallacher, P. Jan, S. Koyiloth Vayalil and H. Patrick, *Langmuir*, 2016, **32**, 2928–2936.
16   C. J. Rasmussen, G. Y. Gor and A. V Neimark, *Langmuir*, 2012, **28**, 4702–4711.
17   H. J. Wang, A. Kleinhammes, T. P. McNicholas, J. Liu and Y. Wu, *J. Phys. Chem. C*, 2014, **118**, 8474–8480.
18   S. H. Zandavi and C. A. Ward, *Phys. Chem. Chem. Phys.*, 2015, **17**, 9828–9834.
19   L. R. Fisher and J. N. Israelachvili, *J. Colloid Interface Sci.*, 1981, **80**, 528–541.
20   M. Kohonen, N. Maeda and H. Christenson, *Phys. Rev. Lett.*, 1999, **82**, 4667–4670.
21   J. Zhong, S. H. Zandavi, H. Li, B. Bao, A. H. Persad, F. Mostowfi and D. Sinton, *ACS Nano*, 2016.
22   D. Sinton, *Lab Chip*, 2014, **14**, 3127–3134.
23   W. Song, H. Fadaei and D. Sinton, *Environ. Sci. Technol.*, 2014, **48**, 3567–3574.
24   R. Fisher, M. K. Shah, D. Eskin, K. Schmidt, A. Singh, S. Molla and F. Mostowfi, *Lab Chip*, 2013, **13**, 2623–2633.
25   B. Bao, J. Riordon, Y. Xu, H. Li and D. Sinton, *Anal. Chem.*, 2016, **88**, 6986–6989.
26   K. Ando, A. Q. Liu and C. D. Ohl, *Phys. Rev. Lett.*, 2012, **109**, 1–5.
27   G. Nagashima, E. V. Levine, D. P. Hoogerheide, M. M. Burns and J. A. Golovchenko, *Phys. Rev. Lett.*, 2014, **113**, 1–8.
28   O. Vincent, D. A. Sessoms, E. J. Huber, J. Guioth and A. D. Stroock, *Phys. Rev. Lett.*, 2014, **113**, 1–5.
29   S. Witharana, B. Phillips, S. Strobel, H. D. Kim, T. McKrell, J. B. Chang, J. Buongiorno, K. K. Berggren, L. Chen and Y. Ding, *J. Appl. Phys.*, 2012, **112**.
30   C. Duan, R. Karnik, M.-C. Lu and A. Majumdar, *Proc. Natl. Acad. Sci.*, 2012, **109**, 3688–3693.
31   A. S. Tucker and C. A. Ward, *J. Appl. Phys.*, 1975, **46**, 4801–4808.
32   R. Zhang, Y. Ikoma and T. Motooka, *Nanotechnology*, 2010, **21**, 105706.
33   S. H. Zandavi and C. A. Ward, *J. Colloid Interface Sci.*, 2013, **407**, 255–264.
34   M. Blander and J. L. Katz, *AlChE J.*, 1975, **21**, 833–848.
35   T. A. Renner, G. H. Kucera and M. Blander, *J. Colloid Interface Sci.*, 1975, **52**, 391–396.
36   J. Ally, S. Molla and F. Mostowfi, *Langmuir*, 2016, **32**, 4494–4499.
37   V. P. Skripov, *Metastable liquids*, John Wiley & Sons, New York. Toronto, 1974.
38   V. E. Vinogradov and P. A. Pavlov, *Int. J. Mod. Phys. B*, 2013, **27**, 1–10.
39   C. Sun, E. Can, R. Dijkink, D. Lohse and A. Prosperetti, *J. Fluid Mech.*, 2009, **632**, 5–16.
40   E. D. Torniainen, A. N. Govyadinov, D. P. Markel and P. E. Kornilovitch, *Phys. Fluids*, 2012, **24**.
41   V. P. Carey, *Liquid-vapor phase-change phenomena*, Taylor & Francis Group, New York. Abingdon, 2008.
42   S. Kelly, M. T. Balhoff and C. Torres-Verdin, *Langmuir*, 2015, **31**, 2167–2179.
43   V. N. Phan, N. T. Nguyen, C. Yang, P. Joseph, L. Djeghlaf, D. Bourrier and A. M. Gue, *Langmuir*, 2010, **26**, 13251–13255.
44   S. Gruener and P. Huber, *Phys. Rev. Lett.*, 2009, **103**.
45   A. Kusmin, S. Gruener, A. Henschel, O. Holderer, J. Allgaier, D. Richter and P. Huber, *J. Phys. Chem. Lett.*, 2010, **1**,

3116–3121.

46   T. Hofmann, D. Wallacher, M. Mayorova, R. Zorn, B. Frick and P. Huber, *J. Chem. Phys.*, 2012, **136**.

47   N. R. Tas, J. Haneveld, H. V. Jansen, M. Elwenspoek and A. Van Den Berg, *Appl. Phys. Lett.*, 2004, **85**, 3274–3276.